Optik - International Journal for Light and Electron Optics 178 (2019) 1163–1176

Contents lists available at ScienceDirect

Optik

journal homepage: www.elsevier.com/locate/ijleo

Original research article

# Synthesis, spectral characterization, DFT and photosensitivity studies of 1-{[(4-methoxy-5-oxo-5*H*-furo [3,2-g]chromen-6-yl) methylidene]amino}-4,6-dimethyl-2-oxo-1,2-dihydropyridine-3-carbonitrile (MFCMP)

N. Roushdy[a], A.A.M. Farag[b,c,*], Magdy A. Ibrahim[d], Shimaa Abdel Halim[d], Nasser M. El-Gohary[d]

[a] *Electronics Materials Dep. Advanced Technology& New Materials Research Inst., City of Scientific Research & Technological Applications (SRTA-City), New Borg El-Arab City, P.O. Box: 21934 Alexandria, Egypt*
[b] *Physics Department, Faculty of Science and Arts, Jouf University, Jouf, Saudi Arabia*
[c] *Thin film laboratory, Physics Department, Faculty of Education, Ain Shams University, Roxy, 11711, Cairo, Egypt*
[d] *Department of Chemistry, Faculty of Education, Ain Shams University, Roxy, 11711, Cairo, Egypt*

ARTICLE INFO

*Keywords:*
Schiff base
TD-DFT calculations
Thin film
Energy gap
Heterojunction
Photosensitivity

ABSTRACT

Condensation reaction of 6-formylvisnagin (**1**) with 1-amino-4,6-dimethyl-2-oxo-1,2-dihydropyridine-3-carbonitrile (**2**) afforded the novel 1-{[(4-methoxy-5-oxo-5*H*-furo[3,2-*g*]chromen-6-yl)methylidene]amino}-4,6-dimethyl-2-oxo-1,2-dihydro-pyridine-3-carbonitrile (**MFCMP**). The structure of this compound was deduced on the basis of it's corrected analytical and various spectral data. The parameters of the structure were extracted by using the DFT/B3LYP/ 6-311G (d,p) premise set. Besides, TD-DFT estimations were used for the interpretation of the electronic absorption. The experimental optical absorption results indicated an allowed direct transition at 2.29 eV, corresponding to the optical band gap of the synthesized compound film, as well as Urbach tail width with the energy of 0.51eV. The electrical characteristics of the heterojunction based **MFCMP** were accomplished in dark and under various intensity levels of illuminations. Both values of the photocurrent and photosensitivity were found to increase with increasing illumination intensity which gives confirmation for the applicability of the studied heterojunction for the optoelectronic devices.

## 1. Introduction

The natural occurring khellin and visnagen, obtained from the fruits and seeds of *Ammi visnaga* L., possess a high antiatherosclerotic and lipid-altering activity [1,2]. Khellin has been used for the photochemotherapeutic treatment of vitiligo and psoriasis [3]. The photoreaction of khellin with DNA has been considered elsewhere [4]. Further, various authors [5–7] have explored that furochromones involve a situation of extensive significance because of their far-reaching manifestation in the plants and their potential employ as pharmaceuticals. Generally, furochromones are known to have anti-inflammatory and analgesic [8–10], antitumor [11] and antimicrobial activities [12]. A standout amongst the most essential classifications of visnagin is 6-formylvisnagin (4-methoxy-5-oxo-5*H*-furo[3,2-g]chromene-6-carboxaldehyde) [13].

* Corresponding author at: Physics Department, Faculty of Science and Arts, Jouf University, Jouf, Saudi Arabia.
*E-mail address:* alaafaragg@edu.asu.edu.eg (A.A.M. Farag).

https://doi.org/10.1016/j.ijleo.2018.09.130
Received 1 August 2018; Received in revised form 23 September 2018; Accepted 24 September 2018

DFT is a universally useful computational method and can be connected to various systems. Moreover, DFT methods are more helpful for certain kinds of computations than others. Furthermore, DFT can be utilized for computations including metals. Several DFT methods, for example, B3LYP, are specially planned for specific applications, previously definite in the literature [14]

DFT-theoretical calculation can be used for the investigation of the optimized geometries of the synthesized compound; 1-{[(4-methoxy-5-oxo-5*H*-furo[3,2-*g*]chromen-6-yl)methylidene]amino}-4,6-dimethyl-2-oxo-1,2-dihydropyridine-3-carbonitrile (**MFCMP**). In addition, the investigation of the influence of solvent polarity on the observed spectra and other important related parameters were facilitated by the calculation of time dependents-DFT [14–15].

In recent times, the electronic and optoelectronic of organic thin film-based devices have a lot of scientific consideration due to its potential innovative applications, the interest of being lightweight and have conceivably minimal effort and cost for the preparation [16,17]. Currently, the small molecular organic semiconductors are a feasible candidate for efficient organic photovoltaics, owing to significant benefits including well-definite molecular structure, certain molecular weight and easily obtained with high purity and controlled through preparation processes [18,19]. Based on these characteristics, earlier studies have realized an achievement of the high efficiency of these small organic structures due to controlling its topography as a thin film, charge carrier mechanism and the energy band gap[20,21]. Amongst numerous small molecular structure, chromone and its derivatives have become one of the greatest broadly energetic material for various applications. The most natural products like chromones and other related structures have rich chemical diversity and their often valuable biological activity[22–24]. Recently, other physical characteristics were checked and proved for chromones as a thin film for optoelectronic device applications[15,25–27]. The results proved that these structures have semiconducting property, thermal stability, sensitive for light, easy for preparation as a thin film with high quality, adherent with the substrates, for device application with various morphological and crystalline structure. As a continuation of these studies, efforts have been done to synthesize the two bioactive furochromone and pyridine moieties in one molecular frame and both Mulliken atomic charges and the parameters of the structure are taken out by using the DFT at B3LYP/ 6-311 G (d,p) premise set. Therefore, part of this work has addressed the preparation and characterization of **MFCMP** thin films. Also, the optical constants are separated from the estimations of the experimental transmittance and reflectance. Finally, the current density-voltage characteristics of the **MFCMP** thin film-based heterojunctions are studied under influence of dark and various illuminations. The influence of the illumination intensity on the main heterojunction parameters are concerned to check the validity of the prepared device for photodiode application.

## 2. Experimental

### *2.1. Preparation and molecular structural characterizations*

A mixture of 6-formylvisnagin (**1**) (0.98 g, 4 mmol) and 1-amino-4,6-dimethyl-2-oxo-1,2-dihydropyridine-3-carbonitrile (**2**) (0.65 g, 4 mmol) in 20 ml of absolute ethanol and then heated for 2 h under reflux. The yellow crystals obtained after cooling were filtered off and crystallized from ethanol to give **MFCMP** as pale yellow crystals.

Melting points were extracted by using a digital Stuart SMP3 apparatus. The infrared spectra were investigated by using spectrophotometer type Perkin-Elmer 293. $^{1}$H NMR and $^{13}$C NMR were measured on Mercury-300BB (300 MHz) and Mercury-400BB (100 MHz), respectively. The instrument type GC-2010 Shimadzu Gas chromatography-mass spectrometer was considered. Perkin–Elmer CHN-2400 was used for investigating the basic microanalyses.

### *2.2. Computational method*

The well-known Khon-Sham's DFT method through the B3LYP method was used for calculations [14]. The detailed about this function and its advantage were described in the literature [14,15]. A full geometry optimization was extracted [15,28] using a Gaussian 09 package [29]. The obtained geometries were imagined either utilizing GaussView 5.0.9 [30] or chemcraft 1.6 [31] software bundles. The vibrational spectral assignment has been performed for FT-IR spectra of **MFCMP** based on the computationally predicted.

### *2.3. Thin film preparation and physical characterizations of **MFCMP***

Thin films of **MFCMP** were grown on corning glasses and single crystalline Si substrates by using Polos spin coater at 600 rpm for 60 s. Prior to the preparation procedure, the substrates were ultrasonically cleaned and followed by a detailed process stated in our previous literature [32]. The topography of the films was acquired by type JEOL-JSM-636 OLA. The size of the particles was estimated by N5 submicron Particle size analyzer model Beckman.

The UV-Vis-NIR Spectrophotometer (JASCO–670) was used to record the transmission and reflection spectra of the prepared films at 300 K. To estimate the characteristics of the **MFCMP** based heterojunction, current-voltage measurements were made using high impedance Keithly 2635 A in dark and under illumination.

## 3. Results and Discussion

### *3.1. Molecular structure and reaction confirmation*

In the present work, condensation reaction of 6-formylvisnagin (4-methoxy-5-oxo-5*H*-furo[3,2-*g*]chromene-6-carboxaldehyde)

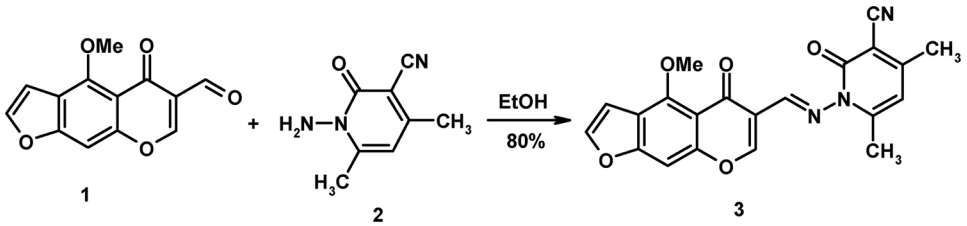


**Scheme 1.** Formation of the novel **MFCMP**.

(**1**) with 1-amino-4,6-dimethyl-2-oxo-1,2-dihydropyridine-3-carbonitrile (**2**) afforded the novel Schiff base identified as 1-{[(4-methoxy-5-oxo-5*H*-furo [3, 2-*g*] chromen-6-yl) methylidene] amino}-4, 6-dimethyl-2-oxo-1,2-dihydropyridine-3-carbonitrile (**MFCMP**) (Scheme 1).

The extracted **MFCMP** as pale yellow crystals were characterizes as : mp 265-266 °C, yield (1.25 g, 80 %). IR (KBr, $cm^{-1}$): 3113 ($CH_{furan}$), 3060 ($CH_{arom.}$), 2959, 2857 ($CH_{aliph.}$), 2218 (C≡N), 1655 (C = $O_{pyridine}$ and C = $O_{\gamma\text{-pyrone}}$), 1597 (C = N), 1538 (C = C). $^1$H-NMR (Fig. 1**(a)**) (300 MHz, DMSO-$_6$): 2.27 (s, 3H, $CH_3$), 2.38 (s, 3H, $CH_3$), 3.93 (s, 3H, $OCH_3$), 6.31 (s, 1H, H-$5_{pyridine}$), 7.04 (s, 1H, H-9), 7.25 (d, 1H, H-$3_{furan}$, *J* = 1.8 Hz), 8.04 (d, 1H, H-$2_{furan}$, *J* = 1.8 Hz), 8.69 (s, 1H, CH = N), 8.99 (s, 1H, H-7). $^{13}$C-NMR (100 MHz, DMSO-$d_6$): 20.0 ($CH_3$), 20.9 ($CH_3$), 58.5 ($OCH_3$), 98.2 (C-9), 105.8 (C-3), 108.3 (C-4a), 113.7 (C-3a), 116.3 (C-6), 116.5 (C≡N), 120.2 (C-$3_{pyridine}$), 129.8 (C-$5_{pyridine}$), 146.4 (C-$4_{pyridine}$), 147.8 (C-$6_{pyridine}$), 148.1 (C-2), 149.3 (C-7a), 151.2 (C-4), 157.0 (C-9a), 157.4 (CH = N), 157.8 (C-7), 164.2 (C = $O_{pyridine}$), 174.4 (C = $O_{\gamma\text{-pyrone}}$). Mass spectrum (Fig. 1 **(b)**), m/z ($I_r$ %): 389 ($M^+$, 2), 242 (100), 227 (92), 212 (76), 195 (28), 186 (73), 176 (25), 160 (24), 148 (83), 132 (17), 119 (84), 105 (21), 92 (13), 78 (25), 65 (17). Anal. Calcd for $C_{21}H_{15}N_3O_5$ (389.36): C, 64.78; H, 3.88; N, 10.79%. Found: C, 64.55; H, 3.70; N, 10.60%.

The structure of **MFCMP** was deduced on the basis of its correct analytical and spectral data. The IR spectrum of **MFCMP** (Fig. 2**(a)**) showed characteristic absorption bands at $\nu_{max}$ 3113 ($CH_{furan}$), 3060 ($CH_{arom.}$), 2959, 2857 ($CH_{aliph.}$), 2218 (C≡N), 1655 (C = $O_{pyridine}$ and C = $O_{\gamma\text{-pyrone}}$), 1597 $cm^1$. Its $^1$H NMR spectrum revealed the presence of singlet signals at2.27 ($CH_3$), 2.38 ($CH_3$), 3.93 ($OCH_3$), 6.31 (H-$5_{pyridine}$), 7.04 (H-9), 8.69 (CH = N), 8.99(H-7), in addition to two doublets assigned to H-$3_{furan}$ and H-$2_{furan}$ at7.25 and 8.04, respectively. The $^{13}$C-NMR of **MFCMP** revealed signals equal to the total numbers of carbon atoms and agrees well with the suggested structure. The spectrum revealed characteristic signals at20.0 ($CH_3$), 20.9 ($CH_3$), 58.5 ($OCH_3$), 116.5 (C≡N), 164.2 (C = $O_{pyridine}$) and 174.4 (C = $O_{\gamma\text{-pyrone}}$). Furthermore, structure of MFCMP was deduced from its mass spectrum which revealed the molecular ion peak at 389 with low abundance ($I_r$; 2%) and the molecule splits into two part which was identified as 6-(iminomethyl)-4-methoxy-5*H*-furo[3,2-*g*]chromen-5-one (m/z 242; 100% as the base peak) and 3-cyano-4,6-dimethyl-2-oxo-1,2-dihydropyridinium cation (148; 83%) The splitting of **MFCMP** during the fragmentation pattern may attribute to the weak N-N bond force.

Comparison of the vibrational frequencies calculated at B3LYP/6-311 G (d,p) with experimental values and corresponding assignment of FT-IR Spectra of the compound are listed in (Table 1) and (Fig. 2 **(b)**). Another attempt to follow up the changes of the **MFCMP** is carried out by studying the vibrational spectra. The calculated frequencies produce a reasonable deviations from the experimental one. This deviation can be attributed to the consideration of the intermolecular interaction for the experimental results in contrary to the theoretical one (i.e. considering the single molecule in the gaseous nature). The scale factor of the calculated vibrational frequencies is equal to 0.9613 at B3LYP/6-311 G(d,p) basis set. The assignment could be achieved extensively as in the following:

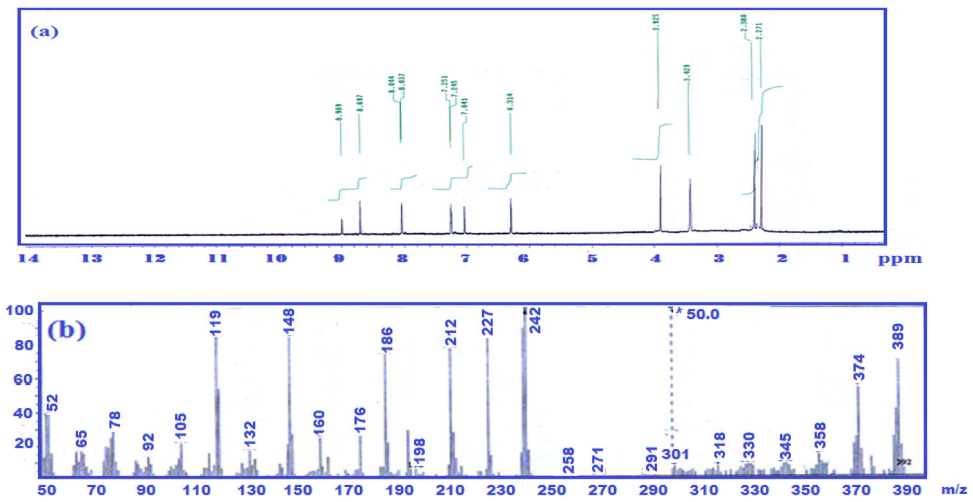


**Fig. 1. (a)**The $^1$H NMR spectrum, and **(b)** The mass spectrum of **MFCMP.**

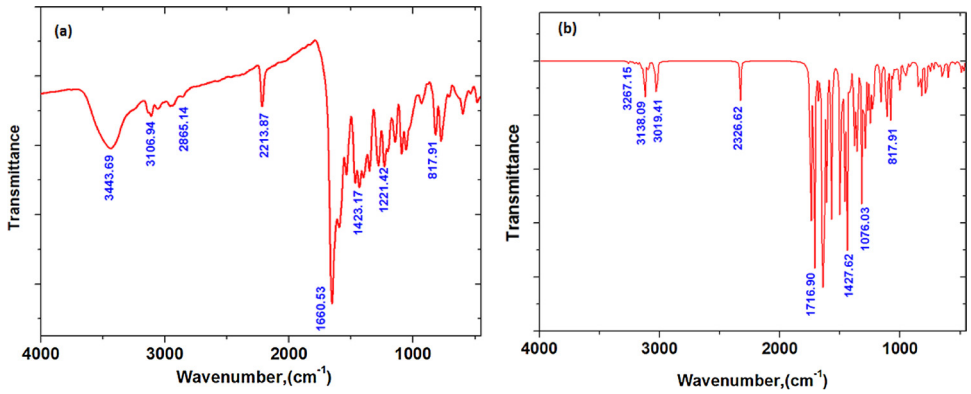


**Fig. 2.** (a) Experimental IR spectrum and (b) Calculated IR spectrum of **MFCMP** at B3LYP/6-311 G (d,p).

**Table 1**
Experimental and computational calculated vibrational wavenumbers (harmonic frequency ($cm^1$)), IR intensities and assignments for **MFCMP** at the B3LYP/6-311 G (d,p).

| No. | Exp. | Wave number | | IR Intensity | | Assigments | References |
|---|---|---|---|---|---|---|---|
| | | unscaled | scaled | Rel. | Abs. | | |
| 1 | 3113 | 3250 | 3124 | 0.745 | 0.523 | υ C-H furan | – |
| 2 | 3060 | 3206 | 3082 | 4.322 | 2.251 | υ C-H aromatic | [22] |
| 3 | 2956, 2857 | 3025 | 2907 | 63.76 | 57.77 | υ C-H aliphatic | – |
| 4 | 1655 | 1713 | 1646 | 379.30 | 225.65 | υ C = O γ-pyrone | [23] |
| 5 | 1597 | 1659 | 1595 | 31.18 | 22.26 | υ C=N | – |
| 6 | 1567 | 1626 | 1563 | 107.86 | 98.36 | β C = C (in ring) | [24] |
| 7 | 2218 | 2308 | 2219 | 47.84 | 34.68 | υ C≡N | – |

$\upsilon_1$ (Stretching); $\upsilon_2$(Symmetric stretching); $\upsilon_3$(Asymmetric stretching); β (In plane bending);

The aromatic C–H stretching vibration [33] is in general observed in the region 3000–3100 $cm^{-1}$.The computed vibration is assigned to C–H aromatic stretching vibration at 3206 $cm^{-1}$ (unscaled value) but (the scaled value at 3082 $cm^{-1}$) which is comparable with experimental results at 3060 $cm^{-1}$. The computed vibration is assigned to symmetric C–H aliphatic stretching vibration in $CH_3$ at 3025 and 3152 $cm^{-1}$ (unscaled value), respectively but the scaled value at 2907 $cm^{-1}$ for the compound has shown a comparable agreement with experimental results at 2956 and 2857 $cm^{-1}$, respectively. The computed vibration is assigned to asymmetric C–H furan stretching vibration at 3250 $cm^{-1}$ (unscaled value) but the scaled value at 3124 $cm^{-1}$ has shown a comparable agreement with experimental results at 3113 $cm^{-1}$. Generally, the C = O vibrations are observed in the region 1790-1810 $cm^{-1}$ [34]. Vibrations are assigned to C = O stretching at 1713 $cm^{-1}$ (unscaled value) but the scaled value at 1646 $cm^{-1}$ which is comparable with experimental result at 1655 $cm^{-1}$. The C = C vibration [33] is observed in the region 1480-1630 $cm^{-1}$. The computed vibration is assigned to C = C stretching vibration at 1626 $cm^{-1}$ (unscaled value) but the scaled value at 1563 $cm^{-1}$ which is comparable with experimental result at 1567 $cm^{-1}$. The computed vibration is assigned to asymmetric C = N [35] stretching vibration at 1659 $cm^{-1}$ (unscaled value) but the scaled value at 1595 $cm^{-1}$ shows a comparable agreement with the experimental result at 1597 $cm^{-1}$. The computed vibration is assigned to C≡N stretching vibration at 2308 $cm^{-1}$ (unscaled value) but the scaled value at 2219 $cm^{-1}$ has shown a comparable agreement with experimental results at 2218 $cm^{-1}$.

### *3.2. Molecular orbital calculations of the ground state energy*

The optimized geometries (i.e., bond lengths, bond angles and dihedral angles) as well as ground state energies; total energy ($E_T$), energy of highest occupied MO ($E_{HOMO}$), energy of lowest unoccupied MO ($E_{LUMO}$), energy gap ($E_g$), dipole moment (μ), and net charges of 1-{[(4-methoxy-5-oxo-5*H*-furo[3,2-*g*]chromen-6-yl) methylidene]amino}-4,6-dimethyl-2-oxo-1,2-dihydropyridine-3-carbonitrile (**MFCMP**) obtained using the B3LYB/6-311 G (p,d) level are presented in Fig. 3 and Tables 2 and 3. Scale factors were suggested for a precise forecast in deciding the zero-point vibrational energies, and the entropy. The diverse in these energies seem to be inadequate. The analysis based on the results of Tables 2 and 3 and Fig. 3 show that: the optimized bond length of C = C in phenyl ring falls in the range from 1.349 to 1.476A° which is in agreement with the experimental data (i.e. 1.481A°) [36] for C = C bonds. The optimized length obtained by B3LYB/6-311 G (p,d) is slightly longer than the experimental data 1.229A° for C = O bonds [36]. The computed bond angles are largely affected by the presence of C = O group in C4, especially < $H_{17}C_{14}O_{15}$, < $N_{33}N_{34}C_{19}$ and < $C_4C_7O_{11}$ are, and (Table 3). The most stable geometry of **MFCMP** is the planar structure, except pyridine moiety (where the dihedral angle $N_{33}N_{34}C_{25}O_{35}$ is 9.16º and $O_{11}C_4C_5C_7$ is −1.87º) are out of the molecular plane of the compound. The Mullikan net charge observed on active centers O and N show a significant change indicating the interaction between different moieties of the

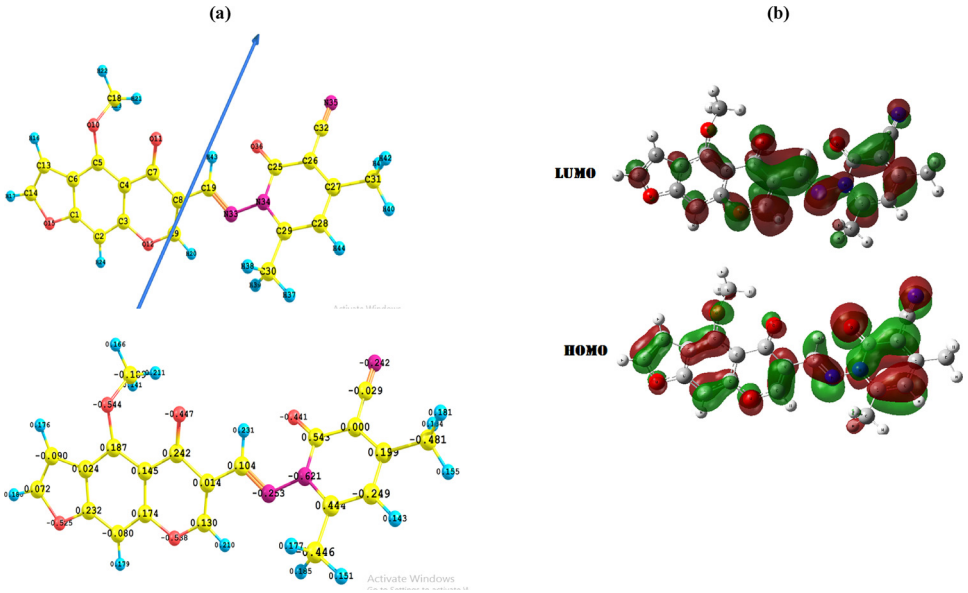


**Fig. 3.** (a) Optimized geometry, numbering system, net charge, vector of dipole moment and (b) HOMO and LUMO of **MFCMP** using B3LYP/6-311 G(d,p).

**Table 2**
The optimized calculations of total energies (a.u.), zero point vibrational energies (kcal. $mol^1$), rotational constants (GHz), entropies (cal.$k^1$), energy of HOMO and LUMO (eV), energy gap (eV) and total dipole moment (Debye) carbonitrile of **MFCMP** at the B3LYP/6-311 G(d,p).

| Parameters | B3LYP/6-311 G(d,p) |
|---|---|
| Total Energy,($E_T$) | |
| Zero Point Vibrational Energy | 203.02185 |
| | 0.46700 |
| Rotational constant | 0.06405 |
| | 0.05973 |
| Entropy | |
| Total | 176.512 |
| Translational | 43.768 |
| Rotational | 36.441 |
| Vibrational | 96.304 |
| Energy of highest occupied molecular orbital ($E_{HOMO}$) | 6.14312 |
| Energy of lowest unoccupied molecular orbital ($E_{LUMO}$) | 2.357424 |
| Energy Gap,($E_g$) | 3.785696 |
| Dipole moment, (μ) | 7.9700 |

compound **(**Fig. 4) and (Table 3**).** The ionization energy, I.E is calculated as 6.14 eV (Table 2). Also, the electron affinity (E.A) is calculated and found to be 2.35 eV. So the calculated energy gap, ($E_g$), is 3.78 eV. Finally, the computed dipole moment (μ) is found to be 7.97 D. In addition, the zero-point vibrational energy of the compound is 203.022 kcal $mol^1$ and total entropy is 176.51 cal.$k^1$ (Table 2).

The distribution of Mulliken atomic charge is implemented in the atomic orbitals of carmoisine [37]. For **MFCMP**, the most electronegative charges are accumulated on N and O, while the most electropositive atoms like C and H have an inclination to accept electrons. The Mullikan's plot of **MFCMP** using B3LYP/ (d,p) method is illustrated in Fig. 4. It is noted from this figure that, the strong negative and positive partial charges on the skeletal atoms of the parent increases with increasing Hammett constant of substituent groups. These allocations of fractional charges on the skeletal atoms demonstrate that the electrostatic repulsive or attractive forces between molecules afford a considerable commitment to the interaction types. A fraction of a particle that has a negative electrostatic potential will be liable to electrophilic attack. It is not as straightforward to use electrostatic potentials to predict the nucleophilic attack. Consequently, the negative district (blue) and positive locale (red) demonstrate electrophilic and nucleophilic assault indications.

### *3.3. Electronic absorption spectra of **MFCMP***

The electronic spectra of **MFCMP** in methanol and xylene solvents and its assignment of spectra are given in Fig. 5. The charge

**Table 3**
Equilibrium bond lengths, bond angles, dihedral angles and net charges of **MFCMP** at the B3LYP/ (p,d) level of theory.

| Bond lengths (Å) | B3LYP/6-311G (p,d) | Bond angle (°) | B3LYP/6-311G (p,d) | Dihedral angles (°) | B3LYP/6-311G (p,d) |
|---|---|---|---|---|---|
| $C_4$—$C_3$ | 1.422 | < $O_{12}C_3C_9$ | 120.110 | < $C_8C_{19}N_{33}N_{34}$ | 174.95 |
| $C_1$—$C_2$ | 1.381 | < $C_6C_5C_4$ | 118.486 | < $H_{20}C_3C_9O_{12}$ | |
| $C_8$—$C_9$ | 1.352 | < $C_1C_2H_{24}$ | 123.669 | < $H_{24}C_1C_2O_{15}$ | |
| $C_{19}$—$C_8$ | 1.460 | < $C_6C_{13}C_{14}$ | 105.817 | < $N_{33}N_{34}C_{25}$ $O_{35}$ | 9.16 |
| $C_{27}$—$C_{31}$ | 1.504 | < $C_4C_7O_{11}$ | 124.366 | < $N_{33}N_{34}C_{29}$ $C_{30}$ | |
| $C_1$—$O_{15}$ | 1.358 | < $C_{13}C_{14}O_{15}$ | 112.164 | < $N_{33}N_{34}C_{19}$ $H_{43}$ | |
| $C_{18}$—$O_{10}$ | 1.440 | < $N_{34}$ $C_{25}O_{36}$ | 120.710 | < $C_{26}$ C $_{27}N_{35}$ $C_{32}$ | 1.85 |
| $C_7$—$O_{11}$ | 1.224 | < $N_{35}$ $C_{32}$ $C_{26}$ | 177.348 | < $C_7$ $C_4$ $C_5$ $O_{11}$ | |
| $C_{13}$—$H_{16}$ | 1.077 | < $N_{33}$ $C_{19}$ $C_8$ | 120.710 | < $C_{27}C_{31}$ $C_{26}$ $H_{42}$ | 67.09 |
| $C_2$—$H_{24}$ | 1.080 | < $C_{28}$ $C_{29}C_{30}$ | 122.333 | **Net charges** | ——— |
| $C_{30}$—$H_{38}$ | 1.093 | < $C_{27}C_{31}$ $H_{40}$ | 111.194 | N | |
| $C_{19}$—$N_{33}$ | 1.284 | < $C_{19}N_{33}N_{34}$ | 116.130 | N | |
| $C_{32}$—$N_{35}$ | 1.156 | < $C_{25}N_{33}N_{34}$ | 119.422 | N | |
| $C_{25}$—$N_{34}$ | 1.444 | < $C_{31}$ H $_{42}$ $H_{40}$ | 108.389 | O | |
| $N_{33}$—$N_{34}$ | 1.401 | < $C_{18}$ O $_{10}$ $H_{22}$ | 105.322 | O | |
| $C_{13}$—$C_{14}$ | 1.349 | < $C_1C_2$ $H_{24}$ | 123.669 | O | |
| $C_7$—$C_8$ | 1.476 | < $C_{13}$ $C_{14}$ $H_{17}$ | 133.037 | O | |
| $C_{18}$—$H_{22}$ | 1.088 | < $C_{14}$ O $_{15}$ $H_{17}$ | 114.799 | O | |

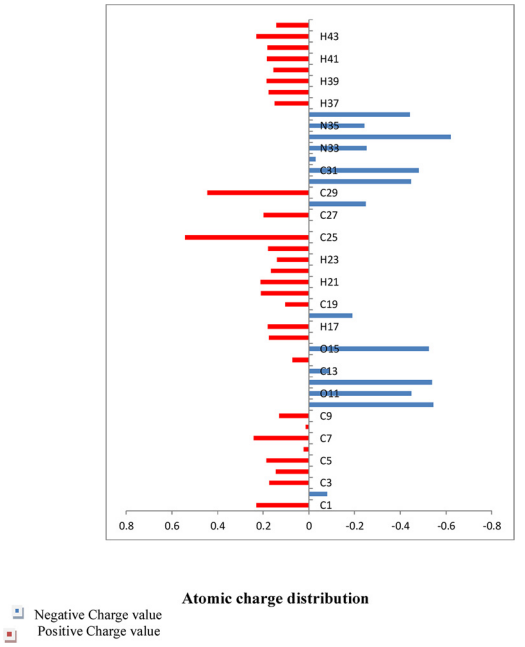


**Fig. 4.** Atomic charge distribution (au) **of MFCMP** using B3LYP/6-311 G(d,p).

density maps of the occupied and vacant MO,s considered in the transitions are presented in Fig. 6. The spectrum in xylene is composed of six bands centered at 393.37, 350.18, 310.79, 286.96, 272.83 and 250.46 nm. Increasing solvent polarity ongoing from xylene to methanol causes small changes in band positions indicating that the polarity of the excited and ground states are of the same values, that is, solvent independent. The excited configurations can be attributed to the electron excitation of eight highest occupied molecular orbital's $\varphi_{94}{}^1\varphi_{101}$ and the lowest four vacant molecular orbital's $\varphi_{102}{}^1\varphi_{105}$. The correspondence between the results of the theoretical and the experimental transitions are satisfactory.

The first $(\pi\text{-}\pi^*)^1$ state is centered at 393.37 nm in xylene this band is predicted theoretically at 389.74 nm, in good agreement with the experiment, and is configurations, namely, $\varphi_{101}{}^1\varphi_{102}$. This band is of CT character from pyridine moiety to the chromone moiety. The second $(\pi\text{-}\pi^*)^1$ state is observed at 350.18 nm in xylene and is predicted theoretically at 342.91 nm and is configurations, namely, $\varphi_{99}{}^1\varphi_{102}$ and $\varphi_{100}{}^1\varphi_{102}$. This band is of CT character from pyridine moiety to the chromone moiety and delocalized. The third $(\pi\text{-}\pi^*)^1$ state is observed in xylene at 310.79 nm and predicted theoretically at 302.57 nm. This band is composed of six configurations, namely, $\varphi_{97}^{-1}$ $\varphi_{102}$, $\varphi_{98}^{-1}$ $\varphi_{103}$, $\varphi_{99}^{-1}$ $\varphi_{102}$, $\varphi_{99}^{-1}$ $\varphi_{103}$, $\varphi_{99}^{-1}$ $\varphi_{104}$, and $\varphi_{101}^{-1}$ $\varphi_{104}$. This band is CT character from chromone moiety to the pyridine moiety, delocalized and localized bands. The fourth $(\pi\text{-}\pi^*)^1$ state computed theoretically at 279.35 nm and observed in xylene at 286.96 nm. This state is composed of a mixture of six configurations as listed in Table 4. Accordingly, charge

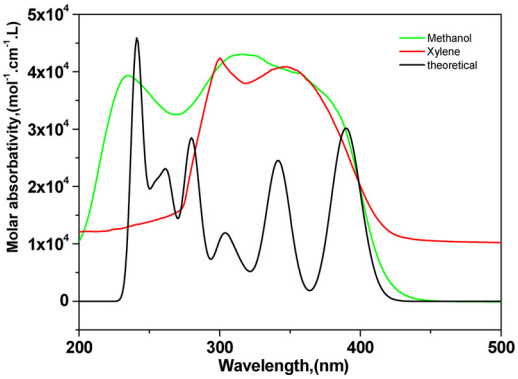


**Fig. 5.** Experimental and electronic absorption spectra of **MFCMP.**

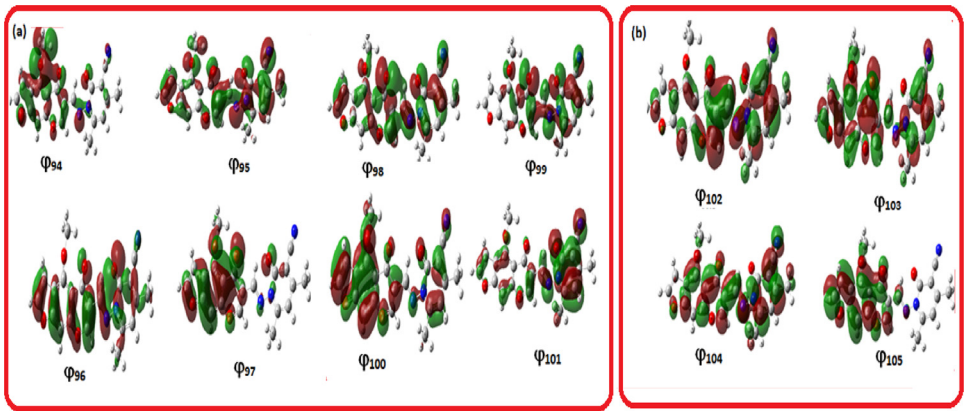


**Fig. 6.** (a) The charge density maps of the occupied, and (b) The charge density maps of the un-occupied states levels of **MFCMP.**

transfer, CT, localized and delocalized configurations can be anticipated. The main contribution of this band is coming from the two configurations $\varphi_{97}^{-1}$ $\varphi_{102}$ and $\varphi_{100}^{-1}$ $\varphi_{104}$, which is of CT character from chromone moiety to the pyridine moiety and delocalized. The fifth $(\pi, \pi^*)^1$ state computed at 272.83 nm in xylene, 267.19 nm in methanol and is computed theoretically at 262.22 nm. This state has a high extremity when contrasted with that of the ground state and consequently dissolvable reliance on band position. This state is composed of a mixture of eight configurations, that is also assigned as a delocalized and a charge transfer band (CT) from pyridine moiety to the chromone moiety (Fig. 6). The last one state computed theoretically, appears at 240.66 nm. This state is composed of a mixture of nine configurations, both states are π-π* and assigned as a delocalized, CT character from chromone moiety to the pyridine moiety and localized transition (Table 4).

### *3.4. Surface morphology characterization*

To obtain information about the surface morphology of **MFCMP** in two different scales of 5 μm and 1 μm, scanning electron microscopy images is illustrated in Fig. 7(a-c). The morphology is composed of many different irregular layer-like structure with the average diameter obtained from a particle size analyzer (shown in Fig. 7 **(d)**) of about 2.3 μm. Some fractures of small sizes are also observed in different orientations and have the same structure and and characterized by an aggregation on the surface of layers. The entire measurement was repeated at various times at randomly picked out sites and the resulting data were considered to be the average.

### *3.5. Optical characterizations of **MFCMP** thin films*

The transmission, T(λ) and reflection, R(λ) spectra of **MFCMP** thin films in a wide wavelength range are shown in Fig. 8. As observed, the films exhibit a transmission increase in the high wavelength region and reaching 92% at 2500 nm. Furthermore, the reflectance decreases at a higher wavelength and reaches 8% at 2500 nm. The observed results for the high transparency in terms of film transparency seem to be better than those obtained by other authors [38,39].

The optical constants, in particular, the refractive index ($n$) and extinction index ($k$) were extracted utilizing the spectrophotometric measurements of T (λ) and R (λ) using the published analysis [38,39]. The optical constant $k$ can be estimated from the absorption coefficient as follows:

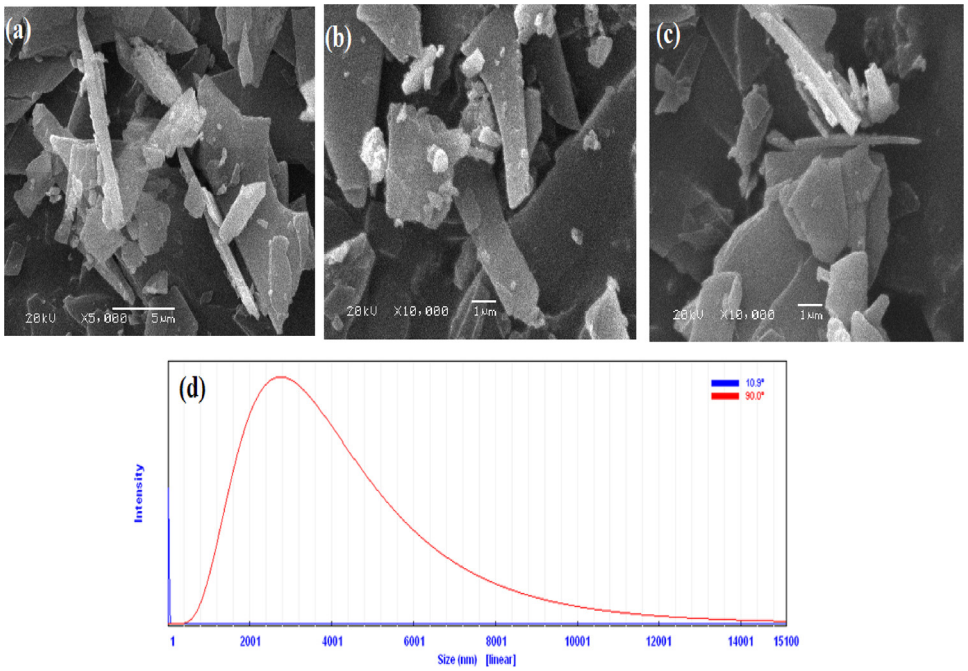


**Fig. 7.** SEM of different magnifications (a) 1000 x, (b) 5,000, (c) 10,000 and (d) Particle size analysis.

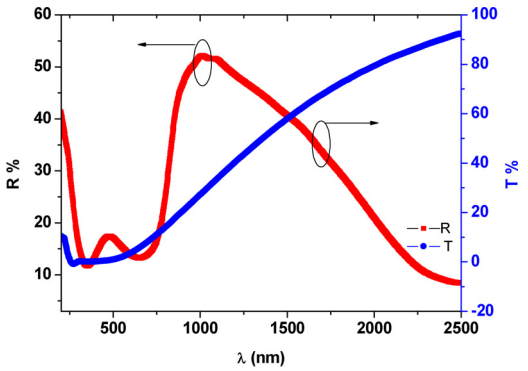


**Fig. 8.** Spectral dependence of R and T characteristics of **MFCMP** thin films.

$$k = \frac{\alpha\lambda}{4\pi}, \tag{1}$$

Where

$$\alpha = \frac{1}{d}\ln\left[\frac{(1-R)^2}{2T} + \sqrt{\left(\frac{(1-R)^4}{4T^2} + R^2\right)}\right], \tag{2}$$

While the refractive index can be extracted using the following equation

$$n = \left(\frac{1+R}{1-R}\right) + \sqrt{\left(\frac{4R}{(1-R)^2} - k^2\right)}, \tag{3}$$

Fig. 9 shows the spectral dependence of both refractive ($n$) and extinction ($k$) indices. As observed, the refractive index, $n$ illustrates, in the absorption region, a type of dispersion called anomalous dispersion, while the dispersion type is normal in the non-absorbing region (transparent region, where $\lambda > 1300$ nm). The obtained optical constants and its behavior are matched with those published for most organic thin films [40–42].

The normal dispersion can be identified from the spectral dependence of a material's refractive index which is commonly expressed by Wemple-DiDomenico formula [43]. The normal dispersion can be explained on the basis of a single oscillator model. But the anomalous dispersion can be caused by the effect of the absorption spectrum in the medium and followed by different modes of

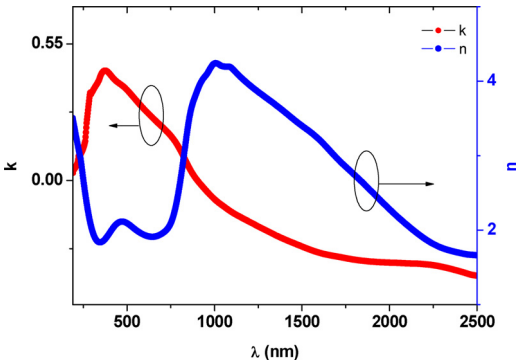


**Fig. 9.** Spectral dependence of extinction index (*k*) and refractive index (*n*) of **MFCMP** thin films.

dispersion and can be explained on the basis of the multi-oscillator model as reported by Iqbal et al.[44] and El-Nahass [45]. This extraordinary attitudes of the refractive index curve against wavelength to the probability of resonance impact of polarization of charge carrier and the incident light spectrum in the absorption region[45].

### 3.6. The optical band gap of *MFCMP* thin films

The information about the kind of transition and determination of the optical energy band gap can be extracted from the analysis of the optical absorption coefficient edge. The photon energy dependence of the absorption coefficient can be expressed as follows [45]:

$$\alpha h\upsilon = B\,(h\upsilon - E_g)^s, \tag{4}$$

where $B$ is constant and $s$ is an exponent used for transition type identification($s$ = ½ or 2 for direct allowed or indirectly allowed transition, respectively). Fig. 10 shows the relationship of $(\alpha h\upsilon)^{1/2}$ against $h\upsilon$ for the studied thin films. The obtained linear fitting confirms that the main type of transition is direct allowed and the energy band gap is determined from the intercepts of the x-axis at $(\alpha h\upsilon)^2 = 0$. Consequently, the obtained value of the optical band gap is 2.29 eV. The contradiction between the theoretical HOMO-LUMO energy difference and the experimental one can be due to some factors that affect the experimental absorption edge like the probability of the occurrence of the imperfection of crystalline bulk, experimental errors of measuring the film thickness and/or an optical constant [46].

The Urbach energy was estimated from the photon energy dependence of the absorption coefficient on the semilogarithmic plot as

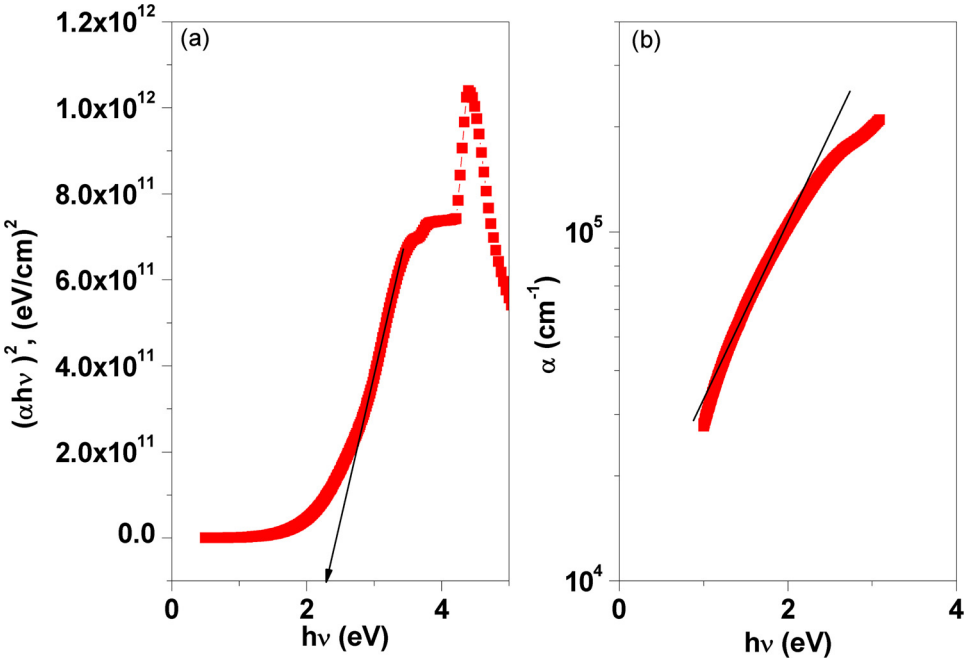


**Fig. 10.** Plot of $(\alpha h\nu)^2$ vs. h $\nu$ of (a) region I and (b) region II of **MFCMP** thin films.

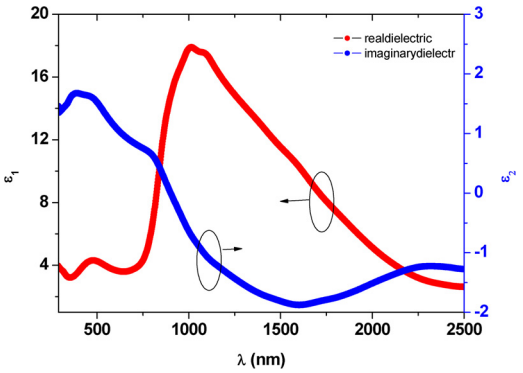


**Fig. 11.** Spectral dependence of real dielectric ($\varepsilon_1$) and imaginary dielectric constant ($\varepsilon_2$) of **MFCMP** thin films.

shown in Fig. 10(b) and found to be 0.51 eV.

### 3.7. Dielectric characterization of *MFCMP* thin films

The dielectric characterization is very important for describing the interaction of the electromagnetic waves through the material molecules [47]. The real dielectric constant can be expressed as follows:

$$\varepsilon_1 = n^2 - k^2 \tag{5}$$

and the imaginary dielectric constant, $\varepsilon_2$, is given by the expression as follows:

$$\varepsilon_2 = 2nk \tag{6}$$

The spectral dependence of both $\varepsilon_1$ and $\varepsilon_2$ is shown in Fig. 11. It can be seen that the value of $\varepsilon_1$ is higher than $\varepsilon_2$ at a certain wavelength through the spectrum. The observed peaks in the spectrum give an indication of charge carrier interaction with the material and characterizing the material.

### 3.8. Nonlinear optical investigations

The nonlinear optics means that the relation of incident light to a material system is no longer linear against the electric field strength. Accordingly, the dielectric polarization, P is nonlinear with respect to the electric field as follows [48]:

$$p(t) = \chi^{(1)} E(t) + \chi^{(2)} E^2(t) + \chi^{(3)} E^3(t) + \cdots \tag{7}$$

where $\chi^{(1)}$, $\chi^{(2)}$ and $\chi^{(3)}$ are the first, second and third order susceptibilities which generally give an indication for the order of nonlinearity are considered to be promising of several applications like electro-optic devices[49].

The linear optical susceptibility is identified with the photon energy by the following expression [49]:

$$\chi^{(1)} = \frac{(n^2 - 1)}{(4\pi)} \tag{8}$$

Third order susceptibility has been studied experimentally in a large variety of materials as homogenous bulk glasses, nano-material, polymers, and can be determined using the following relation[49]:

$$\chi^{(3)} = \frac{A(n^2 - 1)^4}{(4\pi)^4}, \tag{9}$$

where $A$ is a frequency independent quantity and nearly the same for all materials, $A \approx 1.7 \times 10^{-10}$ esu [50]. Fig. 12 illustrates the photon energy dependence of the third-order susceptibility. The results showed a highly broad peak in the near infrared region, in agreement with the photon energy dependence of $\chi^{(1)}$.

### 3.9. Current-voltage characteristics of *MFCMP* / p-Si heterojunction

The schematic diagram for the heterojunction of **MFCMP**/p-Si is shown in Fig. 13. The current density-voltage characteristics of **MFCMP**/p-Si heterojunction in dark and under various illuminations in the range 20-100 mW/cm$^2$ are shown in Fig. 14(a). As observed from the figure that the heterojunction behaves non-linear characteristics that supporting the diode-like behavior with the remarkable rectification characteristics. In addition, the recorded current under illumination is higher than those in dark condition. Furthermore, the reverse current is affected by the illumination intensity larger than those under dark with a remarkable shift towards the forward bias due to the photovoltaic characteristics of the prepared heterojunctions. Such behavior is in agreement with those published for most organic-based heterojunctions [51–53]. Gunduz et al. [54] have interpreted these characteristics by the

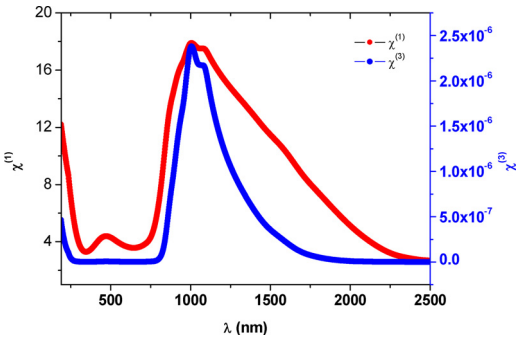


**Fig. 12.** Spectral dependence of $\chi^{(1)}$ and $\chi^{(3)}$ of **MFCMP** thin films.

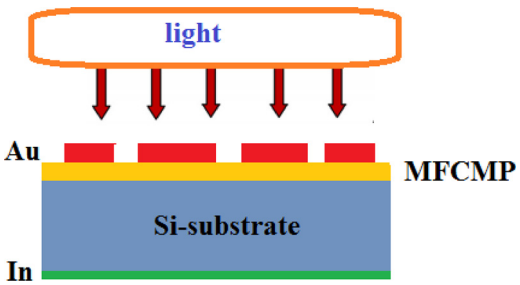


**Fig. 13.** Schematic diagram of **MFCMP**/Si heterojunction under illumination.

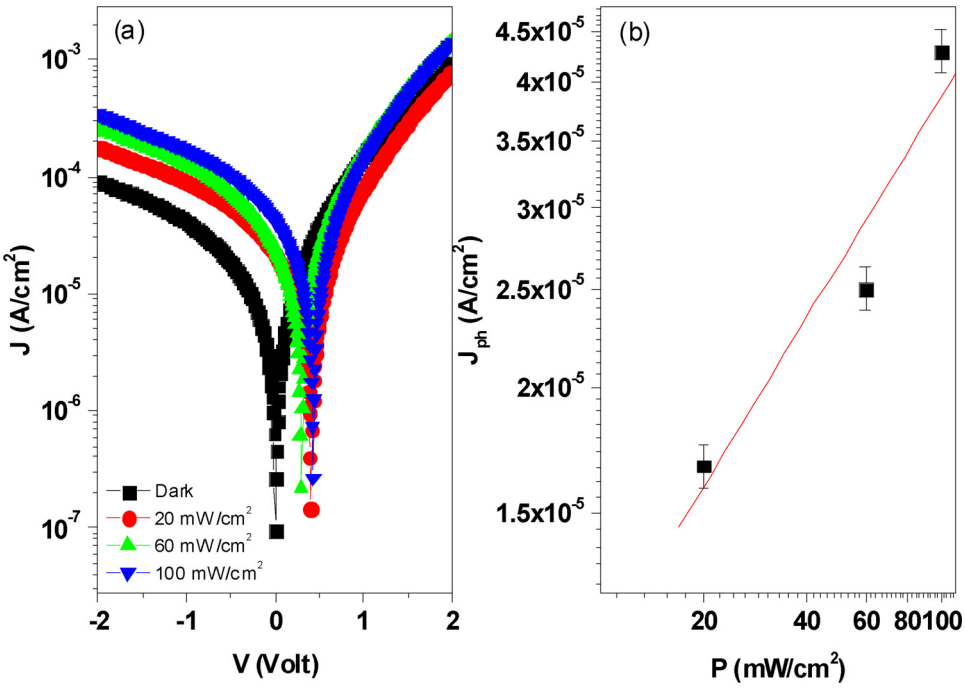


**Fig. 14.** (a) Plot of J vs. V and (b) Plot of $J_{ph}$ vs. P of **MFCMP**/p-Si heterojunction films.

absorption of photons by organic layer and consequently, the photogenerated carriers are adequate to overcome the barrier height and thus increasing the photocurrent. The mechanism is abbreviated as follow: when the organic film is exposed to the photons of the light source under a certain condition, the photon energy is higher than the energy band gap, the charge carriers are generated and separated under effect of built-in potential and then the photocurrent is generated in the external circuit [55]. Fig. 14 (b) shows that the logarithmic plot of photocurrent against light intensity. This figure shows that the photocurrent increases with increasing the illumination intensity which gives support for the photosensitivity of the heterojunction and the applicability for the optical sensor.

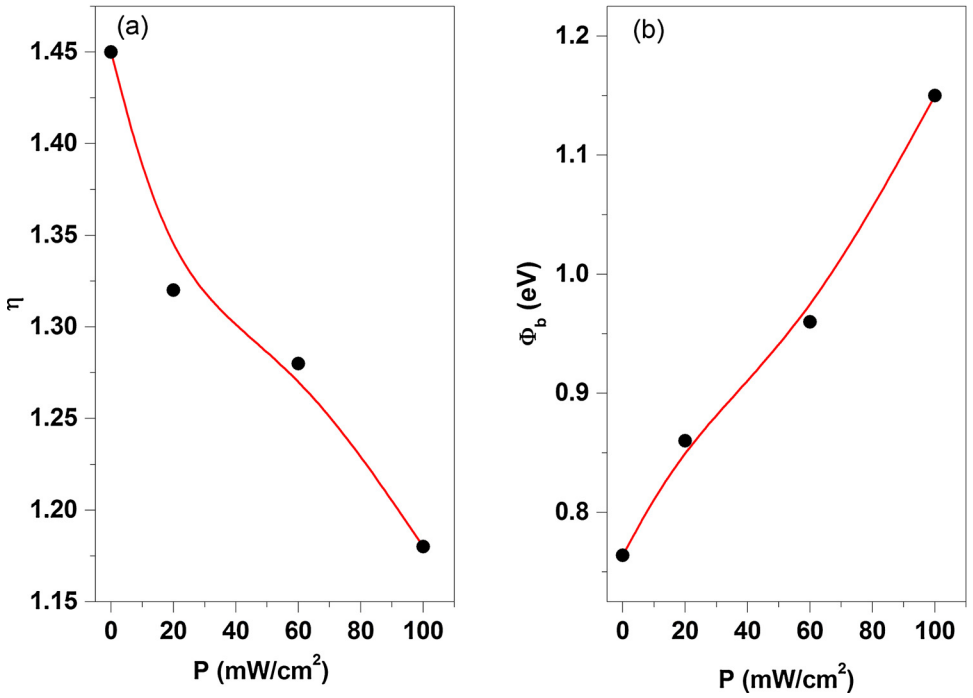


**Fig. 15.** (a) Plot of ideality factor, $\eta$ vs. P and (b) barrier height,$\Phi_b$ vs. P of **MFCMP**/p-Si heterojunction.

The photocurrent as a function of power intensity relationship is expressed as follows [56]:

$$J_{ph} = CP^m, \tag{10}$$

where $J_{ph}$ is the photocurrent, C is constant, m is the exponent for identifying the mechanism and P is the intensity of light. The slope of the curve is found to be 0.65. This value of m lies between 0.5 and 1 which confirming the occurrence of continuous trap distribution levels [57].

The ideality factor, $\eta$ and the barrier height $\Phi_b$ values of the heterojunction were extracted under various illumination intensities as shown in Fig. 15. This figure confirms that the ideality factor decreases while barrier height increases with increasing illumination intensity. The decreasing of the ideality factor with the increasing of light intensity gives an evidence for the enhancement of the diode characteristics under illumination [58,59].

The photocurrent and photosensitivity are measured under the effect of illumination at different applied bias as shown in Fig. 16(a) and (b), respectively. As observed, the photocurrent increases while photosensitivity decreases with increasing applied bias. Moreover, both photocurrent and photosensitivity increase with increasing illumination intensity which gives confirmation for the applicability of the studied heterojunction for the optoelectronic devices [60].

The responsivity of the heterojunction as a function of illumination intensity at different applied bias is shown in Fig. 17(a). The heterojunction shows higher responsivity which increases with increasing the illumination intensity and applied bias. Furthermore, the detectivity of the heterojunction can be calculated from the responsivity using the well-known formula stated in the literature [61,62]. Fig. 17(b) shows illumination intensity dependence of the detectivity at different applied bias. As observed, a significant small increase of the detectivity with increasing illumination intensity while the detectivity decreases with increasing applied bias, in harmony with the previously results by Afify et al. [62] for the photodetector parameters of Ag/TiOPc/p-Si/Al hybrid heterojunction.

## 4. Conclusions

The novel Schiff base of 1-{[(4-methoxy-5-oxo-5*H*-furo[3,2-*g*]chromen-6-yl)methylidene]amino}-4,6-dimethyl-2-oxo-1,2-dihydro-pyridine-3-carbonitrile (**MFCMP**) was obtained using the condensation reaction of 6-formylvisnagin with 1-amino-4,6-dimethyl-2-oxo-1,2-dihydropyridine-3-carbonitrile. The optimized geometries **of MFCMP** obtained using the B3LYB/6-311 G (p,d) level were calculated as 2.35 eV, 3.78 eV, 7.97 D, 203.022 kcal $mol^1$ and 176.51 $cal.k^1$ for the electron affinity, energy gaps, dipole moment, zero-point vibrational energy, and total entropy, respectively. The experimental optical energy gap was found to be 2.29 eV.

The discrepancy between the theoretical and experimental energy gaps was attributed to the influence of the intermolecular interaction for the experimental results contrary to the theoretical one. The presence of various peaks in the spectrum of both real and imaginary dielectric constants of **MFCMP** films gives a suggestion of the charge carrier interaction with the material.

The J-V characteristics of **MFCMP**/p-Si heterojunction in dark and under various illuminations showed diode-like behavior with remarkable rectification characteristics. The trap continuous trap distribution levels mechanism is predominant for the photocurrent

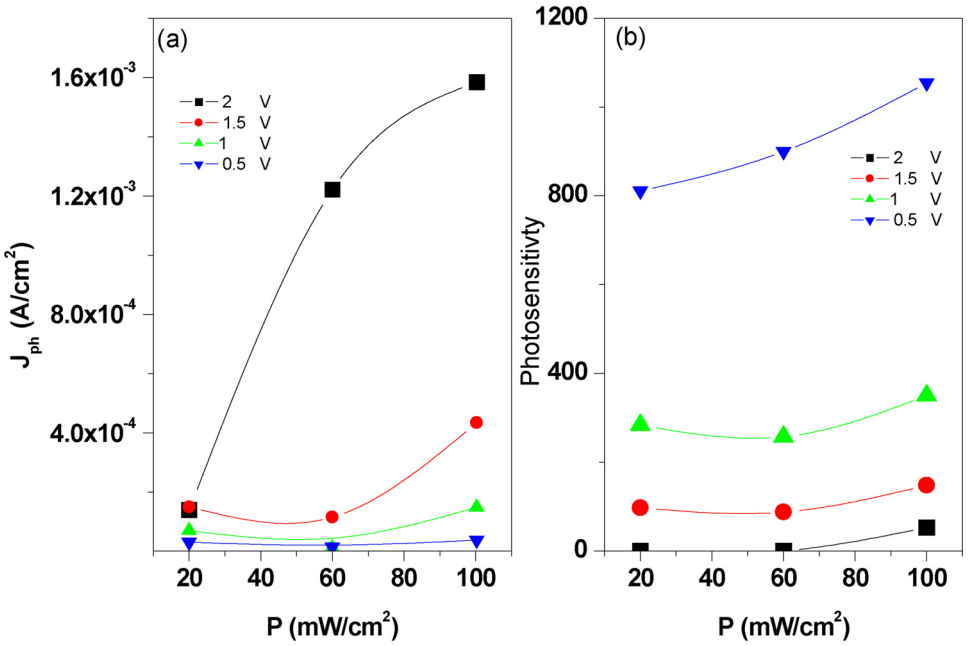


**Fig. 16.** (a) Plot of $J_{ph}$ vs. P and (b) Photosensetivity vs. P of **MFCMP**/p-Si /p-Si heterojunction.

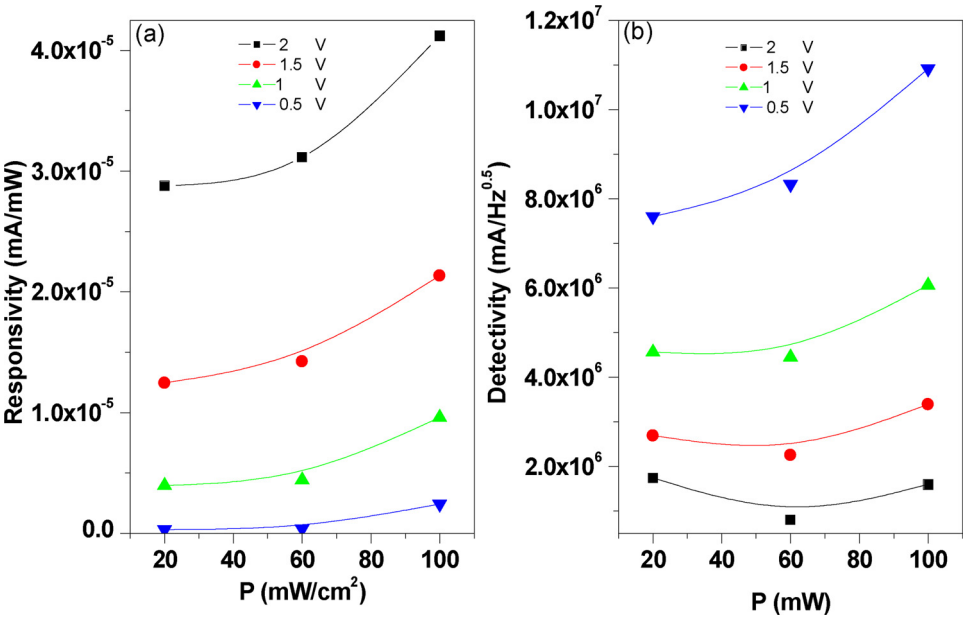


**Fig. 17.** (a) Plot of responsivity vs. P and (b) Detectivity vs. P of **MFCMP**/p-Si /p-Si heterojunction.

under influence of illumination. The photosensitivity characterization of **MFCMP**/p-Si heterojunction under illumination confirm the applicability of this structure for photodiode devices.

## Acknowledgments

The authors would like to thank Physics and Chemistry Departments, Faculty of Education Ain Shams University, as well as Electronics Materials Dep. Advanced Technology& New Materials Research Inst., City of Scientific Research & Technological Applications (SRTA-City), New Borg El-Arab City, Alexandria, Egypt for supporting the scientific results.

## References


[1] A.A. Abu-Hashem, M. El-Shazly, Eur. J. Med. Chem. 90 (2015) 633–665.
[2] R.B. Gammill, C.E. Day, P.E. Schurr, J. Med. Chem. 26 (1983) 1672–1674.
[3] D. Vedaldi, S. Caffleri, F. Dall'Acqua, L. Andrea, L. Bovalini, P. Martelli, Farmaco 4 (1988) 333–346.
[4] L. Trabalzini, P. Martelli, L. Bovalini, F. Dall'Acqua, E. Sage, J. Photochem. Photobiol. B: Bid. 7 (1990) 317–336.
[5] J.S.C. Cox, Adv. Drug Res. 5 (1970) 115–119.
[6] J. Bauer, J.W.T. Selway, J.F. Batchelor, M. Tisdale, I.C. Caldcoell, D.A.B. Young, Nature 292 (1981) 396–400.
[7] H. Ishitsuka, C. Ohsawa, T. Ohiwa, I. Umedo, Y. Suhara, Antimicrob. Agents Chem. Ther. 22 (1982) 611–616.
[8] M. Ghate, M.V. Kulkarni, Indian J. Chem. 44B (2005) 1674–1678.
[9] M.S. Frasinyuk, S.V. Gorelov, S.P. Bondarenko, V.P. Khilya, Chem. Heterocycl. Comp. 45 (2009) 1261–1269.
[10] A.A. Abu-Hashem, M.M. Youssef, Molecules 16 (2011) 1956–1972.
[11] I.F. Zaeid, A.M. Nasef, N.M. Fawzy, A.M. Soliman, M.M. El-Baroudy, Int. J. Pharm. Sci. Rev. Res. 30 (2015) 306–314.
[12] H. Regaila, A. Gohar, G. Abdel Sadek, Egypt. J Pharm. Sci. 29 (1988) 343–347.
[13] F. Eiden, G. Radenmacher, J. Schuenemann, Arch. Pharm. (Weinheim) 316 (1984) 539–547.
[14] (a) A.D. Becke, J. Chem. Phys. 98 (1993) 5648–5652;
(b) A.D. Becke, J. Chem. Phys. 98 (1993) 1372–1377.
[15] Shimaa Abdel Halim, Magdy A. Ibrahim, J. Mol. Struct. 1130 (2017) 543–558.
[16] Y. Li, Y. Chen, T. Yan, M. Lyu, L. Han, Z. Zhang, Y. Li, H. Wang, Y. Li, Nano Energy 46 (2018) 11–19.
[17] S. Vegiraju, Cheng-Ming Hsieh, Deng-Yi Huang, Yen-Chia Chen, Ming-Chou Chen, Dye. Pigment. 133 (2016) 280–291.
[18] H. Mizuno, K. Nagano, S. Tomita, H. Yanagi, I. Hiromitsu, Thin Solid Films 654 (2018) 69–76.
[19] H. Li, L. Li, X. Luan, H. Peng, Y. Zou, Sol. Energy 173 (2018) 1107–1114.
[20] M. Kyeong, Y. Park, A. Gu, H. Kim, S. Hong, Synth. Met. 245 (2018) 10–17.
[21] X. Li, Z. Xu, X. Guo, Q. Fan, Y. Li, Org. Electron. 58 (2018) 133–138.
[22] Sarah A. French, Mitchell R. Clark, Robert J. Smith, T. Brind, Bill C. Hawkins, Tetrahedron 74 (2018) 5340–5350.
[23] Galina F. Makhaeva, Natalia P. Boltneva, Sofya V. Lushchekina, Elena V. Rudakova, Rudy J. Richardson, Bioorg. Med. Chem. 26 (2018) 4716–4725.
[24] Tong-Dong Kuang, Hui-Qin Chen, Fan-Dong Kong, Cai-Hong Cai, Hao-Fu Dai, Phytochem. Lett. 26 (2018) 96–100.
[25] Magdy A. Ibrahim, Shimaa Abdel Halim, N. Roushdy, A.A.M. Farag, Nasser M. El-Gohary, Optik 166 (2018) 294–306.
[26] A.M. Farag, N. Roushdy, Shimaa Abdel Halim, Nasser M. El-Gohary, Sara Said, Spectrochim. Acta Part A 191 (2018) 478–490.
[27] Shimaa Abdel Halim, Magdy A. Ibrahim, N. Roushdy, A.A.M. Farag, Sara Said, Mater. Chem. Phys. 217 (2018) 403–411.
[28] B. B. Stefanov, G. Liu, A. Liashenko, P. Piskorz, I. Komaromi, R. L. Martin, D. J. Fox, T. Keith, M. A. Al-Laham, C. Y. Peng, A. Nanayakkara, M. Challacombe, P. M. W. Gill, B. Johnson, W. Chen, M. W. Wong, C. Gonzalez, J. A. Pople, Gaussian, Inc., Pittsburgh PA, 2003.
[29] M.J. Frisch, G.W. Trucks, H.B. Schlegel, G.E. Scuseria, et al., Gaussian, Inc., Wallingford CT, (2009).
[30] GaussView, Version 5, R.Dennington, T. Keith, J.Millam, Semichem Inc., Shawnee Mission KS, 2009.
[31] http://www.chemcraftprog.com.
[32] M.A. Ibrahim, A.A.M. Farag, N. Roushdy, N.M. El-Gohary, Opt. Mater. (Amst) 51 (2016) 70–77.
[33] J.B. Lambert, H.F. Shurvell, L. Vereit, R.G. Cooks, G.H. Stout, Organic Structural Analysis, Academic Press, New York, 1976.
[34] P.S. Kalsi, Spectroscopy of Organic Compounds, Academic Press, New York, 2018.
[35] R.M. Bassler, G.C. Morrill, T.C. Spectrometric Identification of Organic Compounds. 4th ed. New York: John Wiley and Sons, 1981.
[36] J.N. MacDonald, S.A. Mackay, J.K. Tyler, A.P. Cox, I.C. Ewart, J. Chem. Soc. Faraday Trans. II (77) (1981) 79–89.
[37] M. Snehalatha, C. Ravikumar, I. Hubert Joe, N. Sekar, V.S. Jayakumar, Spectrochim. Acta A. 72 (2009) 654–662.
[38] M.M. El-Nahass, A.F. El-Deeb, H.S. Metwally, H.E.A. El-Sayed, A.M. Hassanien, Solid State Sci. 12 (2010) 552–557.
[39] M.M. El-Nahass, H.A. Afify, A.S. Gadallah, A.M. Hassanien, M.A. Khedr, Mater. Sci. Semicond. Proc. 27 (2014) 254–260.
[40] M.M. El-Nahass, A.M. Hassanien, F.S.H. Abu-Samaha, Eman Elesh, Opt. Commun. 325 (2014) 116–121.
[41] A.A. Abuelwafa, A. El-Denglawey, M. Dongol, M.M. El-Nahass, T. Soga, Opt. Mater. (Amst) 49 (2015) 271–278.
[42] S.H. Wemple, M. DiDomenico, Phys. Rev. B 3 (1971) 1338–1351.
[43] J. Iqbal, I.S. Yahia, H.Y. Zahran, S. AlFaify, A.M. AlBassam, A.M. El-Naggar, Opt. Mater. (Amst) 62 (2016) 527–533.
[44] M.M. El-Nahass, H.M. Abd El-Khalek, A.M. Nawar, Eur. Phys. J. Appl. Phys. 7 (2012) 30201–30213.
[45] D. Prakash, E.R. Shaaban, M. Shapaan, S.H. Mohamed, A.A. Othman, K.D. Verma, Mater. Res. Bull. 80 (2016) 120–126.
[46] P. Lazic, R. Armiento, F.W. Herbert, R. Chakraborty, R. Sun, M.K.Y. Chan, K. Hartman, T. Buonassisi, B. Yildiz, G. Ceder, J. Phys. 25 (2013) 465801.
[47] R. L. Sutherland, D. G. McLean, S. Kirkpatrick, Handbook of Nonlinear Optics Second Edition, Revised and Expanded, Marcel Dekker, Inc, New York, 2003.
[48] R. Adair, L.L. Chase, S.A. Payne, Phys. Rev. B 39 (1989) 3337–3350.
[49] P. Geter (Ed.), Nonlinear Optical Effects and Materials, Springer, 2000.
[50] S. Mansouri, R. Bourguiga, F. Yakuphanoglu, Microelectron. Reliab. 52 (2012) 2585–2591.
[51] R.K. Gupta, A.A. Al-Ghamdi, Omar Al-Hartomi, H. Hasar, Farid El-Tantawy, F. Yakuphanoglu, Synth. Met. 162 (2012) 981–987.
[52] R.K. Gupta, M.E. Aydın, F. Yakuphanoglu, Synth. Met. 161 (2011) 5–2360.
[53] B. Gunduz, I.S. Yahia, F. Yakuphanoglu, Microelectron. Eng. 98 (2012) 41–57.
[54] Bahaa E.A. Saleh, Malvin Carl Teich, Fundamentals of Photonics, John Wiley & Sons, Inc., Hoboken, New Jersey, 2007.
[55] S. Kazim, V. Alia, M. Zulfequar, M. Mazharul Haq, M. Husain, Physica B 3 (2007) 310–315.
[56] F. Yakuphanoglu, B.F. Senkal, Synth. Met. 159 (2009) 311–314.
[57] M. Soylu, M. Cavas, A. Al-Ghamdi, Z.H. Gafer, F. El-Tantawy, F. Yakuphanoglu, Sol. Energy Mater. Sol. Cells 124 (2014) 180–185.
[58] M.A. Ibrahim, A.A.M. Farag, N. Roushdy, N.M. El-Gohary, J. Mol. Str. 5 (2016) 370–380.
[59] I.S. Yahia, F. Yakuphanoglu, S. Chusnutdinowd, T. Wojtowicz, G. Karczewski, Curr. Appl. Phys. 13 (2013) 537–543.
[60] X. Gong, M. Tong, Y. Xia, W. Cai, J.S. Moon, Y. Cao, G. Yu, C.L. Shieh, B. Nilsson, A.J. Heeger, Science 325 (2009) 1665–1667.
[61] J.B. Wang, W.L. Li, B. Chu, C.S. Lee, Z.S. Su, G. Zhang, S.H. Wu, F. Yan, Org. Electron. 12 (2011) 34–38.
[62] H.A. Afify, M.M. El-Nahass, A.S. Gadallah, M.A. Khedr, Mater. Sci. Semicond. Proc. 39 (2015) 324–331.